All-Atom Computer Simulations of Amyloid Fibrils Disaggregation

Jun Wang, Chunhu Tan, Hai-Feng Chen, and Ray Luo
Department of Molecular Biology and Biochemistry, University of California at Irvine, Irvine, California

ABSTRACT Amyloidlike fibrils are found in many fatal diseases, including Alzheimer's disease, type II diabetes mellitus, transmissible spongiform encephalopathies, and prion diseases. These diseases are linked to proteins that have partially unfolded, misfolded, and aggregated into amyloidlike fibrils. The kinetics of amyloidlike fibrils aggregation is still hotly debated and remains an important open question. We have utilized the GNNQQNY crystal structure and high-temperature molecular dynamics simulation in explicit solvent to study the disaggregation mechanism of the GNNQQNY fibrils and to infer its likely aggregation pathways. A hexamer model and a 12-mer model both with two parallel β-sheets separated by a dry side-chain interface were adopted in our computational analysis. A cumulative time of 1 μs was simulated for the hexamer model at five different temperatures (298 K, 348 K, 398 K, 448 K, and 498 K), and a cumulative time of 2.1 μs was simulated for the 12-mer model at four temperatures (298 K, 398 K, 448 K, and 498 K). Our disaggregation landscape and kinetics analyses indicate that tetramers probably act as the transition state in both the hexamer and the 12-mer simulations. In addition, the 12-mer simulations show that the initial aggregation nucleus is with eight peptides. Furthermore, the landscape is rather flat from 8-mers to 12-mers, indicating the absence of major barriers once the initial aggregation nucleus forms. Thus, the likely aggregation pathway is from monomers to the initial nucleus of 8-mers with tetramers as the transition state. Transition state structure analysis shows that the two dominant transition state conformations are tetramers in the 3-1 and 2-2 arrangements. The predominant nucleus conformations are in peptide arrangements maximizing dry side-chain contacts. Landscape and kinetics analyses also indicate that the parallel β-sheets form earlier than the dry side-chain contacts during aggregation. These results provide further insights in understanding the early fibrils aggregation.

INTRODUCTION

Amyloidlike fibrils are found in many fatal diseases, including Alzheimer's disease, type II diabetes mellitus, transmissible spongiform encephalopathies, and prion diseases (1–4). These diseases are linked to proteins that have partially unfolded, misfolded, and aggregated into amyloidlike fibrils. Decades of investigations of the structural properties of amyloidlike fibrils have established that all fibrils have a common structural cross-β spine though few atomic-resolution structures were available from experiment (5,6). Experimental methods are vital in the study of amyloid fibril formation. However, the nature of fibril aggregation, such as limited structural order, insolubility in water, and involvement of cell membrane, makes the experimental study extremely difficult (7,8). Indeed, the fibrils formation mechanism and the aggregation kinetics have remained hotly debated open questions.

Thus, many researchers have turned to computer simulations at various levels of resolutions to gain a better understanding of the molecular-level details in fibrils formation (7,8). Invaluable insights into the fibrils formation mechanisms have been obtained by these computational studies (9–36). Pellarin and Caflisch (18) and Fawzi et al. (22) investigated the kinetics of fibril formation with coarse-grained models. A similar question was also investigated by Nguyen and Hall (11) with their off-lattice intermediate resolution model. An intensive simulation of amyloid β-dimer formation in explicit solvent was presented by Gnanakaran et al. (16), and many interesting findings were reported. More detailed overview of simulations in protein aggregation can be found in recent reviews (7,8).

The lack of experimental atomic-resolution structures is largely due to the noncrystalline and insoluble nature of the amyloidlike fibrils. Recently, the crystal structure of a seven-residue fragment (GNNQQNY) from Sup-35 was released (6). The fragment was found to display all the common characteristics as a full-length Sup-35 protein, including cooperative kinetics of aggregation, fibril formation, and binding of the dye Congo red (6). Further, the crystal structure clearly shows the cross-β spine architecture (6). Subsequent molecular dynamics simulations in explicit solvent from the crystal structure indicate that the cross-β spine architecture is twisted in the absence of crystal packing (37). The GNNQQNY structure, which displays the common cross-β spine structure, represents the best available atomic model for amyloidlike fibrils. If we assume that common structural characteristics for all amyloidlike fibrils imply common mechanism of pathogenesis (38), the study of aggregation in the short GNNQQNY peptide could illustrate some common fundamental mechanism that governs fibril formation in large protein systems.

The timescale of fibrils aggregation is approximately minutes to days (38), which is much longer than the timescale

Submitted February 20, 2008, and accepted for publication August 5, 2008.

Jun Wang and Chunhu Tan contributed equally to this work.

Address reprint requests to Ray Luo, Tel.: 949-824-9528; E-mail: rluo@uci.edu.

Editor: Ruth Nussinov.

0006-3495/08/12/5037/11 $2.00

doi: 10.1529/biophysj.108.131672

of nanoseconds in routine classical all-atom MD simulations. Thus, the challenge in computer simulations of fibrils aggregation is similar to that of protein folding. In protein folding studies, the unfolding rate increases at high temperatures, for example at temperatures as high as 498 K, so that most single-domain proteins unfold in the nanosecond timescale (39). Indeed, high temperature simulations of protein unfolding have been widely used (40,41) to bypass the difficulties in protein folding studies. In the case of protein aggregation, the disaggregation rate should also increase at high temperatures. Thus, it is reasonable to explore the same high-temperature simulation technique to study fibrils aggregation. Nevertheless, care should be used in the protein disaggregation simulations, just as in protein unfolding simulations. For example, it has been pointed out that unfolding pathways are only reverse of folding pathways in a given temperature range (42). Thus, it is important to analyze the effect of temperature in high-temperature disaggregation simulations.

In this study, we have utilized the GNNQQNY crystal structure and molecular dynamics simulations in explicit water at multiple temperatures to understand the disaggregation mechanisms of the GNNQQNY fibrils and to infer its likely initial aggregation pathways. Two models were adopted in our analysis: a hexamer aggregate and a 12-mer aggregate both with two sheets separated by a dry interface (Fig. 1). Cumulatively, 1-μs trajectories at five different temperatures (298 K, 348 K, 398 K, 448 K, and 498 K) were collected for the hexamer model, and 2.1-μs trajectories at four temperatures (298 K, 398 K, 448 K, and 498 K) were collected for the 12-mer model.

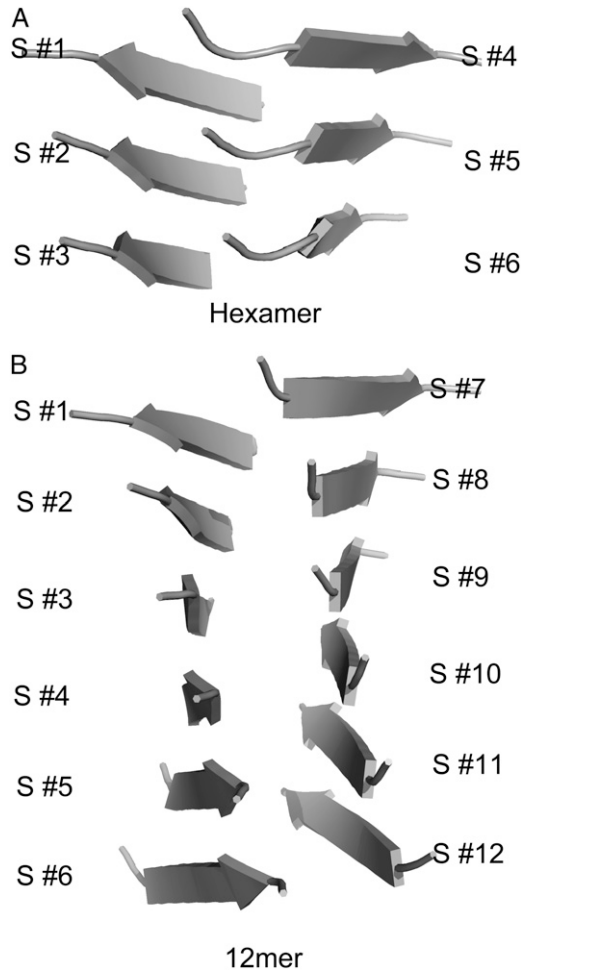

FIGURE 1 Hexamer (*A*) and 12-mer (*B*) models of the GNNQQNY cross-β spline aggregate at 298 K. Both snapshots are the closet to the mean of the production trajectories after equilibration.

METHODS

Room-temperature and high-temperature molecular dynamics simulations

In this work, two cross-β GNNQQNY aggregate models, hexamer and 12-mer, were used to investigate the disaggregation of amyloid fibrils. The initial atomic coordinates of both models were constructed from the crystal structure 1YJP using symmetry operation *P*21 (6). Hydrogen atoms were added using the LEAP module of AMBER8 (43). The hexamer model was solvated in a truncated octahedron box of 3813 TIP3P water molecules so that the final concentration of the system after equilibration is 98 mM, which is at the upper end of the experimental concentration range for crystallization (6). The 12-mer model was solvated with twice as many TIP3P water molecules (7626) to maintain a final concentration similar to that in the hexamer simulation. Particle-mesh Ewald (44) was employed to treat long-range electrostatic interactions with the default setting in AMBER8 (43). A revised parm99 force field was used for intramolecular interactions (45,46). One-thousand-step steepest descent minimization was performed to relieve any structural clash in the solvated system. The SHAKE algorithm (47) was used to constrain bonds involving hydrogen atoms so that a 2-fs time step was used.

The minimized systems were used to start different trajectories at 298 K. Each 298 K trajectory was first simulated with Langevin dynamics with a different random number seed, i.e., each trajectory was started with the same initial structure but with a different initial velocity assignment. At this stage, each trajectory was only briefly equilibrated for 20 ps in the NVT ensemble. The friction constant was set to be 1 ps^{-1}. Each of the Langevin dynamics trajectories was then followed by a 20-ns molecular dynamics trajectory in the NPT ensemble at 298 K and 1 bar, which were used as reference (i.e., the aggregated state) to study the high-temperature disaggregation pathways. Totally 10 independent trajectories for the hexamer model and 20 independent trajectories for the 12-mer model were collected at 298 K. It was found that 10 ns per trajectory was sufficient to equilibrate both the hexamer and 12-mer model at the room-temperature simulation condition, so that the second 10 ns was used for data analysis.

Disaggregation for the hexamer model was studied with 10 independent trajectories per temperature at four different temperatures: 348 K (40 ns each), 398 K (20 ns each), 448 K (10 ns each), and 498 K (10 ns each). Sampling is more challenging in the 12-mer simulation due to its higher stability. Here twice as many (20) independent trajectories were simulated per temperature. It is found that doubling of trajectories from 10 to 20 does not change the qualitative conclusions in the landscape analyses (see Supplementary Material, Fig. S8 in Data S1). This indicates that sampling at the chosen temperatures is sufficient in the 12-mer simulations. Nevertheless, only three different temperatures were used for the 12-mer model: 398 K (57 ns each), 448 K (22 ns each), and 498 K (8 ns each) since the 12-mer aggregate is too stable at 348 K to collect enough disaggregation snapshots within reasonable CPU time. The simulation times were set to be long enough to reach the disaggregated equilibration phase (i.e., 100% monomers) in all except the 12-mer simulation at 398 K, where only 75% monomers were reached. In all high-temperature simulations the NVT ensemble was used to keep the water density fixed at the value of 298 K, i.e., each high-temperature NVT trajectory

was started from the end of a corresponding trajectory at 298 K. Note that both the initial structures and initial velocities were different among all high-temperature trajectories. Cumulatively 1000 ns were collected at 298 K, 348 K, 398 K, 448 K, and 498 K for the hexamer model, taking ~9500 CPU hours on the in-house dual-core dual-processor Xeon 5410 (2.33 GHz) cluster. For the 12-mer model, cumulatively 2100 ns were collected at 298 K, 398 K, 448 K, and 498 K, taking ~43,700 CPU hours.

β- and dry native contact identification

As shown in Fig. 1 the native contacts in the two model aggregates can be classified into two categories: β- and dry contacts. The β-contacts are defined as in-register C_α-C_α contacts between a pair of strands within each of the two β-sheets, including contacts between strands #1 and #2, strands #2 and #3, strands #4 and #5, and strands #5 and #6. If the distance of an in-register C_α-C_α contact is less than the cutoff distance of 6 Å, it is identified as a β-contact. A total of 28 β-contacts can be identified for the hexamer model, and a total of 56 β-contacts can be identified for the 12-mer model. The dry contacts are defined as side-chain-to-side-chain contacts between a pair of strands at the dry interface. For example, there exist dry contacts between strands #1 and #4, strands #1 and #5, strands #2 and #5, strands #2 and #6, and strands #3 and #6 for the hexamer model. If the distance between the centers of mass of any two side chains at the dry interface is less than the cutoff distance of 5 Å, it is identified as a dry contact. A total of 15 dry contacts can be identified for the hexamer model and 33 dry contacts can be identified for the 12-mer model. Note that not every contact is stable at room temperature. For example, on average 25.9 stable β-contacts and 8.8 stable dry contacts for the hexamer model were found in all 10 independent trajectories at 298 K.

Contacts per pair of strands

The β- and dry contacts identified above apparently belong to a pair of strands. Thus, the number of contacts per pair of strands can be computed for later identification of aggregate. Note that a total of seven β-contacts exist between a pair of strands within a β-sheet, and a total of three dry contacts exist between a pair of strands at the dry interface. At room temperature, the average numbers of contacts per pair of strands at the two interfaces are different from the maximum values and can be found in Tables S1 and S2 in Data S1 for the hexamer model and the 12-mer model, respectively.

Aggregate identification

The aggregate identification process can be cast as a graph problem if we regard each strand as a vertex (48). An edge between any two vertices exists if there are sufficient contacts (either β or dry) between the two strands (vertices). Thus, the question becomes, using the hexamer model as an example, how many connected components can be found in a graph with six vertices, and how many vertices are in each component? Here a connected component is an aggregate, ranging from one to six vertices (strands). Therefore, the first step in the aggregate identification process is to find out which pair of strands has enough contacts. That is to say, the first step is to build-up the adjacency matrix representation of the graph. This is achieved by monitoring the total contacts per pair of strands in each trajectory as shown above. We have empirically chosen 80% of total contacts per pair of strands at the room-temperature as cutoff, i.e., two strands are in contact (in other words, an edge exists between the two vertices) if their total contacts are >80% of their 298 K value. The corresponding element of adjacency matrix is set to 1 when the two strands are in contact.

At the second step, a recursive procedure of depth-first search method (48) is used to find out how many vertices are in a connected component, i.e., how many strands are in an aggregate. The number is termed ''order of aggregate'', ranging from monomers (1) to hexamers (6) for the hexamer simulations and from monomers (1) to 12-mers (12) for the 12-mer simulations. (See Fig. S4 in Data S1 for a list of all conformations for all possible aggregates for the hexamer model.) As shown in Fig. S4 in Data S1, there is one conformation for hexamers, three for pentamers, five for tetramers, three for trimers, and two for dimers. Identification of all possible aggregates for the 12-mer model follows similarly, although it is far more complicated.

RESULTS AND DISCUSSION

An important issue in the study of amyloidlike fibrils is the identification of initial aggregation nucleus. The relative ease in simulating many independent disaggregation trajectories at high temperatures allows quantitative analyses to be applied to answer this question, at least from the disaggregation perspective. In the following, we intend to answer this question first by landscape analyses then by kinetics analyses.

Disaggregation landscape

To understand the disaggregation pathway, the disaggregation landscapes (i.e., $\ln P(x)$) are first analyzed with a progress variable, order of aggregate (x). The values of x correspond to the number of peptides in an aggregate, i.e., 1 = monomer, 2 = dimer, 3 = trimer, . . ., and so on as defined in Methods. Here the probability ($P(x)$) is computed as the percentage of snapshots with the value of x in all the independent simulation trajectories. Figs. 2 and 3 show the landscapes for the hexamer and the 12-mer simulations, respectively. The maximum is found to be around tetramers in the hexamer simulations at all four temperatures and in the 12-mer simulations at all three temperatures. The maximum at tetramers is particularly pronounced at lower simulation temperatures for both models. This indicates that the tetramer aggregates probably act as the transition state at the room temperature in both the hexamer and the 12-mer simulations. In the hexamer simulations, the barriers from monomers to hexamers are 5.23 kT, 5.65 kT, 5.81 kT, and 5.34 kT at 348 K, 398 K, 448 K, and 498 K, respectively. From hexamers to monomers, the corresponding

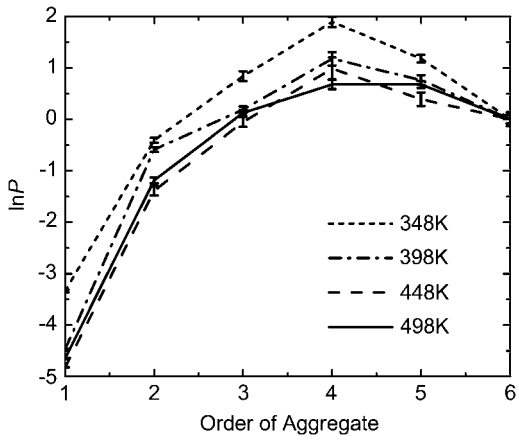

FIGURE 2 Hexamer landscape (relative $\ln P$) versus the order of aggregate at four high simulation temperatures. The value of hexamers is set as reference. The uncertainties are obtained by the jackknife approach. Uncertainty of the first data point is too small to be seen.

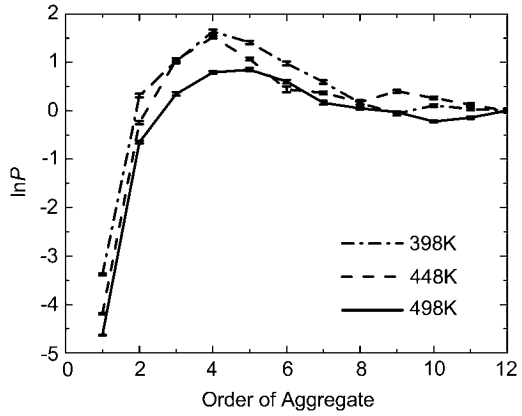

FIGURE 3 12-mer landscape (relative ln$P$) versus the order of aggregate at three high simulation temperatures. The value of 12-mers is set as reference. The uncertainties are obtained by the jackknife approach. Uncertainty of the first data point is too small to be seen.

barriers are 1.89 kT, 1.17 kT, 0.99 kT, and 0.69 kT. As expected, the barrier from hexamers to monomers decreases when temperature increases in the disaggregation process. However, the barrier from monomers to hexamers first increases with temperature up to 448 K, then it decreases when temperature increases from 448 K to 498 K. In the 12-mer simulations, the barriers from 12-mers to monomers are 1.64 kT, 1.51 kT, and 0.84 kT at 398 K, 448 K, and 498 K, respectively, in qualitative agreement with the trend observed in the hexamer simulation. The barriers from monomers to 12-mers were not calculated because the 12-mers did not disaggregate 100% into monomers at 398 K. Further, the 12-mer simulations indicate that the initial nucleus, i.e., the first stable aggregate, is with at least eight peptides. More interestingly, the landscape from 8-mer to 12-mer is quite flat. This is the case at all three simulation temperatures.

Nelson et al. hypothesized that the initial nucleus/intermediate state for the GNNQQNY aggregation is approximately four peptides (6). However, our landscape analysis shows that the tetramer aggregates act as the transition state in both the hexamer and the 12-mer simulations, which disagrees with the hypothesis by Nelson et al. (6). The 12-mer simulations further indicate that the initial nucleus is with at least eight peptides. Our explicit-solvent simulations at high temperatures should be compared with a recent simulation study of Fawzi et al., where they showed that the nucleus of $A\beta_{1-40}$ chains is an aggregate of 10 peptides in their room temperature simulations with a coarse-grained model (22). Another simulation by Nguyen et al. indicates that the nucleus is larger than six $A\beta_{16-22}$ chains (28). Besides simulation studies, experimental evidence also suggests that there are more than seven chains for the nucleus of the $A\beta_{1-40}$ fibrils (38). Thus, the observation of the tetramer aggregates as the transition state in both the hexamer and 12-mer simulations is not due to the use of the high-temperature simulation conditions. Further, the initial nucleus turns out to be higher-ordered aggregates that are more stable than the tetramer aggregates. Interestingly, Gsponer et al. showed that the initial nucleus of the GNNQQNY fibrils may be a three-peptide β-sheet based on their three-peptide simulations (49). Apparently, their simulation system is too small to observe any higher-ordered nuclei. Our landscape analysis further shows that the dimer aggregate is not a thermodynamically stable state. A recent MD study by Zheng et al. (50) also shows that the dimer aggregate is unstable. For $A\beta_{1-42}$, dimers were not observed by mass spectrometry or unstable in simulations (51,52).

To gain a more detailed understanding of the disaggregation mechanisms, we have also studied the disaggregation landscape with respect to the two peptide interfaces in the crystal structure, i.e., the β-sheet main-chain contacts (β-contacts) and the dry side-chain contacts (dry contacts) as identified in the crystal structure (6). Two native contact fractions, Q_β (β-contact fraction) and Q_d (dry contact fraction) as defined in Methods, are used to monitor the interface disaggregation progress. The calculation of the landscape is similar to that of the landscape with respect to the order of aggregate. The disaggregation landscape with respect to the two interfaces (see Fig. S1 in Data S1) suggests that dry contacts disrupt earlier than β-contacts. (Only interface analyses for the hexamer simulation are shown. The interface analyses for the 12-mer simulation yield conclusions qualitatively similar to those from the hexamer simulation; data not shown.) This is consistent with our kinetics analysis of the two interfaces below and the hypothesis by Nelson et al. based on their crystal structure that the dry interface forms later than the β-sheet (6).

Disaggregation kinetics

The disaggregation mechanisms for the two model systems were further analyzed from a kinetics perspective. We made two assumptions to simplify the kinetics analysis of the complex systems. The first assumption is that only one peptide dissociates from a given aggregate at any given time in the disaggregation trajectories. This assumption turns out to be quite reasonable: we analyzed all saved snapshots for both the hexamer and the 12-mer simulations and found that only $\sim$2.0% snapshots in the 12-mer simulations and $<$1.0% snapshots in the hexamer simulations violate the assumption. The second assumption is that the disaggregation of any aggregate is an irreversible first-order reaction at the high-temperature simulation condition, i.e., the order of aggregate at any given time only decreases as simulation proceeds. Apparently, this further reduces the complexity of the disaggregation kinetics analysis. Our detailed snapshot analysis shows that $\sim$1.1% snapshots in the 12-mer simulations and $<$0.7% snapshots in the hexamer simulations undergo an aggregation.

Given the two assumptions, we have the following kinetic model for the 12-mer model:

$$\begin{aligned} M_{12} &\xrightarrow{k_{12}} M_{11} + M_1 \\ M_{11} &\xrightarrow{k_{11}} M_{10} + M_1 \\ &\vdots \\ M_2 &\xrightarrow{k_2} 2M_1. \end{aligned} \quad (1)$$

Here M_i represents an i-mer aggregate of i monomers and k_i is the corresponding reaction rate. The kinetic model for the hexamer model follows similarly. Further, we may use the following system of ordinary difference equations (ODEs) to model the concentration changes of all aggregates in the disaggregation kinetics,

$$\begin{aligned} \frac{d[M_{12}]}{dt} &= -k_{12}[M_{12}] \\ \frac{d[M_{11}]}{dt} &= k_{12}[M_{12}] - k_{11}[M_{11}] \\ &\vdots \\ \frac{d[M_2]}{dt} &= k_3[M_3] - k_2[M_2] \\ \frac{d[M_1]}{dt} &= k_2[M_2] + \sum_{i=2}^{12} k_i[M_i], \end{aligned} \quad (2)$$

where $[M_i]$ is the concentration of M_i . If the rate constants k_i and the initial concentrations of aggregates are known, we can calculate the concentrations of aggregates at any time. Thus, we can optimize a set of rate constants that yield the best agreement between the aggregate concentrations from the ODE system and the aggregate concentrations estimated from the all-atom simulation trajectories.

In this study, the rate constants in the ODE system (Eq. 2) were optimized by minimizing the root-mean squared deviation between the time-dependent aggregate concentrations (note that concentrations from all simulations were approximated with aggregate percentages, but with stoichiometry considered) from Eq. 2 and those from simulations. Obviously, a brute-force systematic search of all rate constants is an exponentially hard problem, especially for the 12-mer kinetics. Fortunately, the concentrations of higher-order aggregates only depend on a few rate constants. For example, $[M_{12}]$ only depends on k_{12} and $[M_{11}]$ only depends on k_{12} and k_{11}. Therefore, we first estimated all rates successively, in the order of k_{12}, k_{11}, k_{10}, ... , and k_1. This was followed by a systematic refinement to fine-tune all rate constants.

The final optimized rate constants are listed in Table 1 and the fitted curves along with the simulation data are plotted in Fig. 4 for the hexamer simulation and Fig. 5 for the 12-mer simulation. An apparent observation is that the tetramer aggregates overall have the highest rate constant in the hexamer simulations; and in the 12-mer simulations the highest rates are mostly found at the trimer and tetramer aggregates; consistent with the landscape analysis, it shows that these states are most in transit during disaggregation. Furthermore, rate constants k_8, k_9, k_{10}, k_{11}, and k_{12} are very similar in the 12-mer simulations, corresponding to their roughly equal probabilities of occurrence as shown in its landscape analysis (Fig. 3). Thus aggregates of 8-mer to 12-mer are meta-stable during the disaggregation process of the 12-mer model, indicating that they are the possible nuclei/intermediate states in its disaggregation. Specifically, the eight-peptide aggregate is probably the smallest nucleus in the process.

More importantly the ''transit'' nature of the tetramer aggregates are independent of the models used in the simulations, indicating that the tetramer aggregates probably play the role of transition state in the initial nucleation of the GNQQNY fibrils. The temperature-dependence of the analyses shows that the above conclusions probably still hold at the room temperature.

Classical analysis of the hexamer kinetics

We also tested two competing classical kinetics models to confirm the absence of intermediate state in the hexamer kinetics. Here the time-dependent concentrations of aggregates in two competing kinetics models are first discussed: one without the intermediate state and one with the intermediate state. These are followed by kinetics fitting to both models to validate the absence of intermediate state in the hexamer kinetics.

Two-state transition

In this kinetics model, hexamers directly disaggregate into monomers without any intermediate state. Thus we have

$$H \xrightarrow{k_{61}} 6M, \quad (3)$$

where H is hexamer, M is monomer, and k_{61} is the forward rate. The corresponding rate equations are

TABLE 1 Kinetic rates fitted with respect to Eq. 2

	k_2	k_3	k_4	k_5	k_6	k_7	k_8	k_9	k_{10}	k_{11}	k_{12}
Hexamer, 348 K	0.17	0.31	0.90	0.41	0.19						
Hexamer, 398 K	0.80	0.90	2.4	1.9	1.2						
Hexamer, 448 K	1.6	3.5	12	6.3	5.7						
Hexamer, 498 K	6.0	16	23	19	16						
12-mer, 398 K	0.25	0.31	0.38	0.30	0.20	0.17	0.13	0.11	0.15	0.14	0.13
12-mer, 448 K	1.0	2.8	2.9	1.4	0.80	0.79	0.48	0.60	0.52	0.53	0.48
12-mer, 498 K	6.5	7.2	6.1	4.5	3.2	2.2	1.7	1.7	1.5	1.7	1.8

All rates were sampled with two significant digits, corresponding to 1.0% relative uncertainty in the fitted values. The root mean-squared absolute deviations between fitted and simulation percentages are $<2.0\%$ for the hexamer simulations, and $<1.1\%$ for the 12-mer simulations.

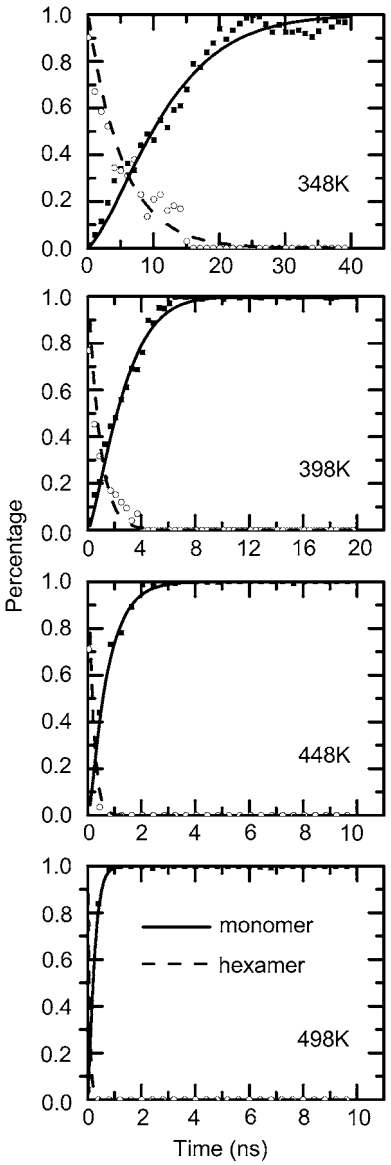

FIGURE 4 Kinetics of monomers (*solid lines*/*solid dots*) and hexamers (*dash lines*/*open dots*) in the hexamer simulations from simulations (*dots*) and from Eq. 2 (*lines*). A total of 40 ns data per trajectory were used for 348 K, 20 ns for 398 K, and 10 ns for 448 K and 498 K, respectively. Each simulation data point was block-averaged over 0.4 ns and all 10 trajectories. The standard error for each data point is plotted as uncertainty, which is too small to be seen.

$$\frac{d[M]}{dt} = 6k_{61}[H], \tag{4}$$

$$[H](0) = [H_0], \tag{5}$$

$$C = [M] + 6[H], \tag{6}$$

where $[H_0]$ is the concentration of H at the beginning of disaggregation and C is the total protein concentration in term of monomers. Here the solution is

$$[H] = [H_0]e^{-k_{61}t}, \tag{7}$$

$$[M] = 6[H_0](1 - e^{-k_{61}t}). \tag{8}$$

Clearly, both $[H]$ and $[M]$ follow single-exponential kinetics with an apparent rate constant k_{61}.

Consecutive three-state transition

In this kinetics model we further assume that tetramers, T, act as intermediate as hypothesized by Nelson et al. based on their crystal structure (6). Thus we have

$$H \xrightarrow{k_{64}} T + 2M \xrightarrow{k_{41}} 6M, \tag{9}$$

where k_{64} and k_{41} are the forward rates for the first and second transitions, respectively. The corresponding rate equations are

$$\frac{d[H]}{dt} = -k_{64}[H], \tag{10}$$

$$\frac{d[M]}{dt} = 4k_{41}[T] + 2k_{64}[H], \tag{11}$$

$$[H](0) = [H_0], \tag{12}$$

$$C = [M] + 4[T] + 6[H]. \tag{13}$$

Here the solutions are

$$[H] = [H_0]e^{-k_{64}t}, \tag{14}$$

$$[M] = Pe^{-k_{64}t} + Qe^{-k_{41}t} + C, \tag{15}$$

where

$$P = \frac{2(k_{64} - 3k_{41})[H_0]}{k_{41} - k_{64}}, \tag{16}$$

$$Q = -P - C. \tag{17}$$

Comparing Eqs. 7 and 8 with Eqs. 14 and 15, the most important difference between the two kinetics models is the function forms for $[M]$, one or two exponential terms. This is similar to protein folding. The high-temperature disaggregation simulation data at all four different temperatures was fitted to both kinetics models to test which one is more suitable. Our analysis shows that $[M]$ at all four temperatures can be represented well by single-exponential functions as shown in Fig. S2 in Data S1. This suggests that the disaggregation process can be described by the first-order kinetics at the high-temperature simulation conditions. For monomers, the half-times are 11.60 ns, 2.47 ns, 0.73 ns, and 0.25 ns at 348 K, 398 K, 448 K, and 498 K, respectively. For hexamers, the half-times are 6.83 ns, 1.19 ns, 0.20 ns, and 0.10 ns, respectively. Clearly, the rate of disaggregation increases with temperature. The independence of kinetics with respect to temperature indicates that the room-temperature kinetics of hexamer disaggregation is probably also first-order by the classical kinetics analysis.

Disaggregation kinetics of two interfaces

To gain a more detailed understanding of the disaggregation kinetics, we have also studied the kinetics of the two interfaces

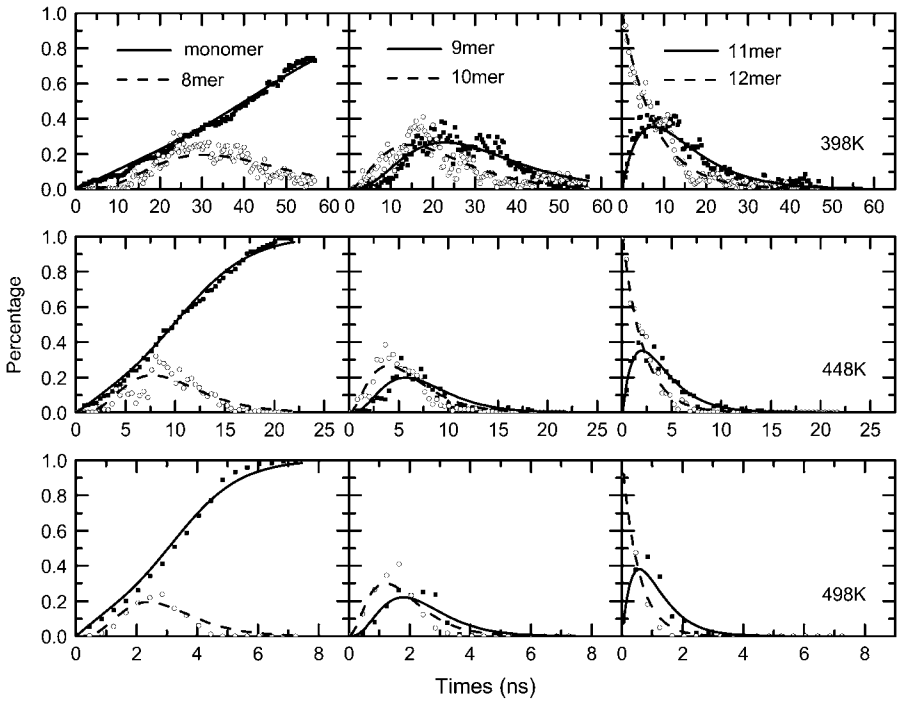

FIGURE 5 Kinetics of monomers and 8-mers (*left*), 9-mers and 10-mers (*center*), and 11-mers and 12-mers (*right*) in the 12-mer simulations from simulations (*dots*) and from Eq. 2 (*lines*). Here, solid circles are for solid lines; and open circles are for dash lines. A total of 57 ns data per trajectory were used for 398 K, 22 ns for 448 K, and 8 ns for 498 K, respectively. Each data point was block-averaged over 0.4 ns and all 20 trajectories. The standard error for each data point is plotted as uncertainty, which is too small to be seen.

for the hexamer model: the β main-chain contacts and the dry side-chain contacts in the original crystal structure (6). Two native contact fractions (Q_β and Q_d) are used to monitor the interface disaggregation kinetics. Time evolutions of Q_β and Q_d at all four temperatures are shown in Fig. S3 in Data S1. Overall, their disaggregation processes can be represented well by single-exponential functions, indicating that all processes obey first-order kinetics at the high-temperature simulation conditions. Fig. S3 in Data S1further shows that Q_d decays faster than Q_β at all four temperatures, suggesting that dry interface disrupts more quickly than that of the β-sheet, consistent with the above landscape analysis of the two interfaces.

Transition state analysis

The landscape analyses above show that there probably is one transition state corresponding to the maximum along the disaggregation pathway whether the hexamer or the 12-mer model was used in the simulations. Clearly, the maximum corresponds to the tetramer aggregate (apparently this is not according to the brute-force *p*50 rule, which is extremely difficult to simulate in explicit solvent). Using the hexamer model as an example, we studied the transition state (TS) structures discovered in the landscape analyses. We scanned MD snapshots for TS structures, or tetramers, in all independent trajectories at each simulation temperature, 348 K, 398 K, 448 K, and 498 K, respectively. At 348 K a total of 2230 snapshots out of 400 ns were found at TS. As shown in Fig. S4 in Data S1 (discussed in Methods), a total of five conformations are possible for the tetramer aggregate. Our analysis shows that Tetramer (1) and Tetramer (3) are the most popular conformations. The distribution of Tetramer (1–5) at 348 K is as follows: 1191, 29, 814, 8, and 188. Interestingly, the distribution is qualitatively the same at other temperatures, i.e., with Tetramer (1) and Tetramer (3) being the most popular conformations. At 398 K the distribution is 613, 90, 789, 1, and 25. At 448 K the distribution is 151, 61, 490, 0, and 63. At 498 K the distribution is 73, 5, 125, 1, and 2. It is interesting to note that Tetramer (1) is more sensitive to the simulation temperature than Tetramer (3), especially at lower simulation temperatures, as expected from the arrangement of the peptides (Fig. S4 in Data S1). The temperature-dependence of the two conformations also indicates that Tetramer (1) is probably the predominant transition state structure at room temperature.

Fig. 6 illustrates the two representative conformations (closest to the mean conformations) at TS at 348 K. Fig. 6 *A*

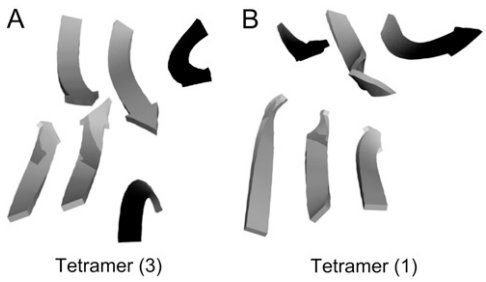

FIGURE 6 Representative transition state conformations at 348 K. (*A*). Tetramer (1). (*B*). Tetramer (3). Here, shading represents aggregated peptides, and solid represents disaggregated peptides.

shows a snapshot of Tetramer (1), where three strands aggregate into a twisted parallel β-sheet with β-contacts and the fourth strand aggregates to the sheet with dry contacts, i.e., the 3-1 arrangement. Fig. 6 *B* shows a snapshot of Tetramer (3), where four strands aggregate into two twisted parallel β-sheets (i.e., the 2-2 arrangement), which are separated by the dry interface.

Meta-stable nuclei/intermediate states

Our landscape and kinetics analyses show that possible meta-stable nuclei or intermediate states exist in the 12-mer simulations. These meta-stable aggregates appear to be 8-mers through 11-mers regardless of temperatures in the 12-mer simulations. More interestingly their probabilities of occurrence are all quite similar to that of the 12-mer aggregates (Fig. 3), i.e., the landscape is rather flat from 8-mers to 12-mers. This can be attributed to their highly similar rates constants as shown in Table 1. We scanned MD snapshots for these meta-stable structures, i.e., 8-mers to 11-mers, in all 20 independent trajectories at each simulation temperature, 398 K, 448 K, and 498 K, respectively. Similar to the situation in the transition state analysis, multiple conformations are possible for any of these meta-stable aggregates. Our analysis shows that the distribution of 8-mers at 398 K is as follows: 4 (the 6-2 arrangement), 6129 (5-3), and 123,115 (4-4). The distribution is qualitatively the same at other temperatures, i.e., with the 4-4 arrangement being the most popular conformation. At 448 K the distribution is 113 (6-2), 3058 (5-3), and 33,010 (4-4). At 498 K the distribution is 0 (6-2), 1603 (5-3), and 8377 (4-4). Only two conformations in the 6-3 and 5-4 arrangements were observed for 9-mers, with the 5-4 arrangement being the overwhelmingly popular one. Similarly for 10-mers, two conformations in the 6-4 and 5-5 arrangements were observed, with the 5-5 arrangement being the dominant one. Only one conformation in the 6-5 arrangement was observed for 11-mers in the 12-mer simulation. Overall these meta-stable nuclei appear to prefer conformations with as many dry side-chain contacts as possible.

It is interesting to point out that the dominance of conformations that maximize dry side-chain contacts is much more pronounced at lower temperatures. This temperature-dependent behavior indicates that these types of arrangements are probably the predominant nucleus structures at room temperature. Fig. 7 illustrates the representative conformations (closest to the mean conformations) for these nuclei at 398 K. Note that the parallel β-sheet structures are not similar to the open or closed β-barrels as reported previously (21,33,34). In addition, the β-sheet content of these nucleus/intermediate state conformations is higher than those reported previously (21,33,34). It can be argued that the high β-sheet content might be due to the high concentration used. However, the concentration used in this work is within the literature values. Specifically the concentrations in the literature (21,33,34) are very similar to that used in this work. Therefore, the observed differences in the nucleus structures between the literature (21,33,34) and this work are less likely to be due to the concentrations used, and more likely to be due to the different protein models used.

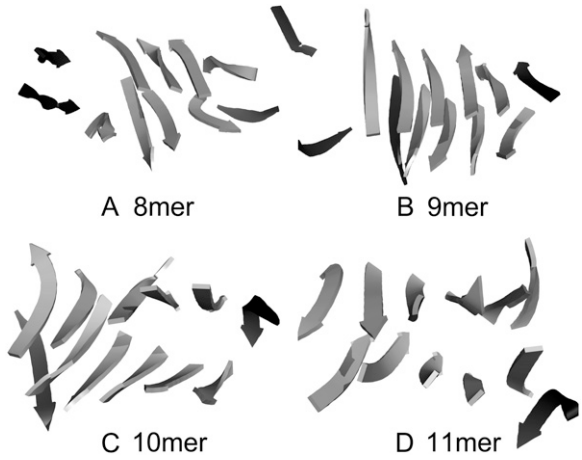

FIGURE 7 Representative nucleus/intermediate state conformations at 398 K. (*A*) 8-mer with four disaggregated peptides; (*B*) 9-mer with three disaggregated peptides; (*C*) 10-mer with two disaggregated peptides; and (*D*) 11-mer with one disaggregated peptide. Here, shading represents aggregated peptides, and solid represents disaggregated peptides.

Finally, it should be pointed out that the conformations of larger nuclei, with the 11-mer nucleus being the extreme case, are likely to be undersampled due to the use of the 12-mer model. A simulation of much larger model may sample other possible conformations at the chosen simulation temperatures.

Disaggregated state

All high-temperature simulations eventually reach the disaggregated equilibrium state except the 12-mer simulation at 398 K. At the disaggregated state, there are neither native β-contracts nor dry contacts. This suggests that all peptides are separated from each other and form random coil.

Aggregated state

As a reference for the above disaggregation simulations, multiple independent trajectories of 20.0 ns each were simulated at 298 K to analyze the aggregated state. Interestingly the twisted parallel β-sheet arrangement is already apparent in the hexamer model (Fig. 1 *A*) and even more so in the 12-mer model (Fig. 1 *B*) as previously observed in a molecular dynamics simulation of a much larger aggregate (37). The average interstrand distance is $\sim$4.88 $\pm$ 0.33 Å and the average intersheet distance is $\sim$9.15 $\pm$ 0.19 Å throughout the simulations, in agreement with experimental observations (6).

The room-temperature stability for the hexamer model, in term of root mean-squared fluctuation of C_α atoms, was also studied and shown in Fig. S5 in Data S1. The data indicates

that all peptides behave qualitatively similarly with low main-chain fluctuation at the five central residues and with high main-chain fluctuation at the two terminal residues, suggesting that the central residues are more rigid than the terminal residues. This is in agreement with the report of Zheng et al. (50). Note that the fluctuation of Asn-6 and Tyr-7 is higher than that of Gly-1 and Asn-2 in strands #1 and #3 (*strand labels* are shown in Fig. 1), but the fluctuation of Asn-6 and Tyr-7 is lower than that of Gly-1 and Asn-2 in strands #4 and #6, consistent with the observation of twisted β-parallel sheets.

To further monitor the interactions responsible for the hexamer stability at the aggregated state, interstrand hydrogen bonds and dry interface contacts were studied. As shown in the structure from Nelson et al., any two adjacent GNQQNY strands in the same sheet form 11 hydrogen bonds. The populations of the 11 hydrogen bonds between strand #1 and #2 are shown in Fig. S6 in Data S1. Clearly, seven of them are stable and four are not. The hydrogen bonds between the following pairs of residues are stable:

Gln-4(#1) and Gln-11(#2);
Gln-4(#1) and Gln-12(#2);
Asn-2(#1) and Asn-10(#2);
Asn-3(#1) and Asn-10(#2);
Gln-4(#1) and Asn-10(#2);
Asn-6(#1) and Gln-12(#2); and
Asn-6(#1) and Asn-13(#2).

The hydrogen bonds between other β-strands are also studied and very similar populations are observed (data not shown). The populations of nine unique dry contacts (those between strands #1 and #4, strands #1 and #5, and strands #2 and #5) are shown in Fig. S7 in Data S1. Six stable dry contacts can be found with populations $>75\%$. The stable dry contacts include:

Gln-4(#1) and Gln-25(#4);
Asn-9(#2) and Asn-34(#5);
Gln-4(#1) and Gln-32(#5);
Gln-11(#2) and Gln-32(#5);
Asn-2(#1) and Asn-27(#4); and
Asn-6(#1) and Asn-30(#5).

The remaining three dry contacts are rather unstable. Note that contacts between strands #2 and #6 are very similar to those between strands #1 and #5, and contacts between strands #3 and #6 are very similar to those between strands #1 and #4 (data not shown). These stable hydrogen bonds and dry contacts should be the major driving forces for stability and aggregation.

Disaggregation pathways and possible aggregation pathways

The disaggregation simulations at 348 K, 398 K, 448 K, and 498 K for the hexamer model and those at 398 K, 448 K, and 498 K for the 12-mer model indicate that the disaggregation mechanisms are not dependent on temperature, though activation barriers are different. This shows that the disaggregation of GNNQQNY aggregates at 298 K may follow qualitatively the same pathways. If we assume that aggregation is the reverse of disaggregation, the proposed aggregation pathway is from monomers to the first meta-stable 8-mer nucleus/intermediate state with tetramers acting as the transition state, as depicted in Fig. 8. Once the eight-peptide nucleus/intermediate state is reached, there are no more significant activation barriers separating it from higher-order nucleus.

Two dominant transition state conformations are Tetramer (1) and Tetramer (3) (Fig. 6). The temperature-dependence of the two conformations indicates that Tetramer (1) is probably the preferred transition state structure at room temperature. This is also consistent with the interface landscape analysis (Fig. S1 in Data S1) and kinetics analysis (Fig. S3 in Data S1) that β-sheet forms earlier than the dry interface. The smallest meta-stable nucleus/intermediate state is with eight peptides (Fig. 7). This is followed by 9-mers, 10-mers, and 11-mers before reaching the 12-mer aggregates. The preferred nucleus conformations are those that maximize dry side-chain contacts. This is especially the case at lower temperatures, indicating these types of conformations are probably the predominant nucleus conformations.

It should be pointed out that a limitation of any explicit solvent simulations of protein aggregation is the small aggregate sizes that have to be used to collect enough simulation data within reasonable CPU time. This is the case even when high temperatures are used. Thus, this study does not exclude other possibilities of kinetic pathways that involve higher-order aggregates. In addition, we cannot exclude the possibilities that disaggregation pathways are different from aggregation pathways, though the conclusions from our high-temperature all-atom simulations in explicit solvent are

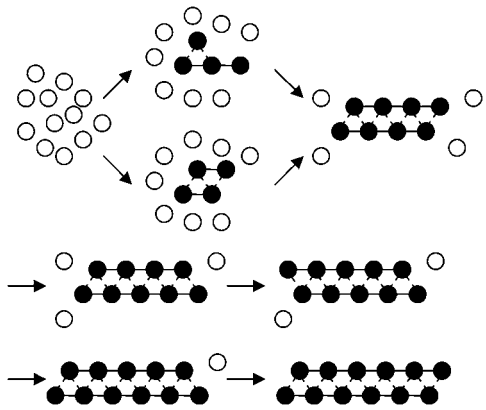

FIGURE 8 Proposed aggregation pathway. The β-contacts are shown as solid lines; dry contacts are shown as dashed lines. Here, solid circles represent aggregated peptides; open circles represent disaggregated peptides.

qualitatively consistent with previous room-temperature simulations in more efficient protein models. Finally both landscape and kinetics analyses depend on the choice of order parameters or observables. This is the case for both simulation and experiment. Here we have chosen a natural progress variable, order of aggregate, in our analysis of the GNNQQNY aggregation. Obviously, different order parameters can be chosen in the above analyses to gain understanding from different angles. For example, we have conducted landscape and kinetics analysis with respect to Q_d and Q_β to understand the interplay of dry and β-contacts in the disaggregation of the hexamer model.

CONCLUDING REMARKS

We have utilized the GNNQQNY crystal structure and high-temperature molecular dynamics simulation in explicit solvent to understand the disaggregation mechanisms of a GNNQQNY hexamer model and a 12-mer model with two parallel β-sheets separated by a dry interface. Cumulatively, 1 μs trajectories were collected for the hexamer model at five different temperatures (298 K, 348 K, 398 K, 448 K, and 498 K), and 2.1 μs trajectories were collected for the 12-mer model at four temperatures (298 K, 398 K, 448 K, and 498 K). The disaggregation landscape indicates that tetramers probably act as the transition state for both the hexamer and the 12-mer simulations. Additionally, the landscape of the 12-mer simulations shows that the initial aggregation nucleus is with eight peptides. Furthermore, the landscape is rather flat from 8-mers to 12-mers indicating the absence of major barriers once 8-mers form. Our kinetics analyses are consistent with the landscape analyses. The proposed aggregation pathway is from monomers to the first meta-stable 8-mer nucleus/intermediate state with tetramers acting as the transition state. Once the eight-peptide nucleus/intermediate state is reached, there are no more significant activation barriers separating it from higher-order nucleus. The two preferred transition state conformations are Tetramer (1) in the 3-1 arrangement and Tetramer (3) in the 2-2 arrangement. The predominant nucleus conformations are in peptide arrangements maximizing dry side-chain contacts. In addition, our simulations also indicate that the parallel β-sheets form earlier than the dry interface during aggregation. Our analysis of the aggregated state indicates that all β-strands behave similarly with low main-chain fluctuation at the five central residues and with high main-chain fluctuation at the two terminal residues, suggesting that the central residues are more rigid than the terminal residues. Population analysis of hydrogen bonds shows that most of them are stable with populations $>75\%$. Analysis of side-chain contacts shows most of them are stable with populations $>75\%$. These stable hydrogen bonds and side-chain contacts should be the major driving forces for stability and aggregation.

SUPPLEMENTARY MATERIAL

To view all of the supplemental files associated with this article, visit www.biophysj.org.

This work is supported in part by the National Institutes of Health (grant No. GM069620).

REFERENCES

1. Dobson, C. M. 1999. Protein misfolding, evolution and disease. *Trends Biochem. Sci.* 24:329–332.
2. Koo, E. H., P. T. Lansbury, and J. W. Kelly. 1999. Amyloid diseases: abnormal protein aggregation in neurodegeneration. *Proc. Natl. Acad. Sci. USA.* 96:9989–9990.
3. Prusiner, S. B. 1997. Prion diseases and the BSE crisis. *Science.* 278: 245–251.
4. Selkoe, D. J. 2002. Alzheimer's disease is a synaptic failure. *Science.* 298:789–791.
5. Sipe, J. D., and A. S. Cohen. 2000. Review: History of the amyloid fibril. *J. Struct. Biol.* 130:88–98.
6. Nelson, R., M. R. Sawaya, M. Balbirnie, A. O. Madsen, and C. Riekel. 2005. Structure of the cross-β spine of amyloid-like fibrils. *Nature.* 435:773–778.
7. Ma, B. Y., and R. Nussinov. 2006. Simulations as analytical tools to understand protein aggregation and predict amyloid conformation. *Curr. Opin. Chem. Biol.* 10:445–452.
8. Hall, C. K., and V. A. Waggner. 2006. Computational approaches to fibril structure and formation. *Amyloid, Prions, Other Protein Aggr. B.* 412:338–365.
9. Demarco, M. L., and V. Daggett. 2004. From conversion to aggregation: protofibril formation of the prion protein. *Proc. Natl. Acad. Sci. USA.* 101:2293–2298.
10. Nguyen, H. D., and C. K. Hall. 2004. Molecular dynamics simulations of spontaneous fibril formation by random-coil peptides. *Proc. Natl. Acad. Sci. USA.* 101:16180–16185.
11. Nguyen, H. D., and C. K. Hall. 2005. Kinetics of fibril formation by polyalanine peptides. *J. Biol. Chem.* 280:9074–9082.
12. Lipfert, J., J. Franklin, F. Wu, and S. Doniach. 2005. Protein misfolding and amyloid formation for the peptide GNNQQNY from yeast prion protein Sup35: simulation by reaction path annealing. *J. Mol. Biol.* 349:648–658.
13. Wu, C., H. Lei, and Y. Duan. 2005. Elongation of ordered peptide aggregate of an amyloidogenic hexapeptide NFGAIL observed in molecular dynamics simulations with explicit solvent. *J. Am. Chem. Soc.* 127:13530–13537.
14. De La Paz, M. L., G. M. S. De Mori, L. Serrano, and G. Colombo. 2005. Sequence dependence of amyloid fibril formation: insights from molecular dynamics simulations. *J. Mol. Biol.* 349:583–596.
15. Boucher, G., N. Mousseau, and P. Derreumaux. 2006. Aggregating the amyloid a β(11–25) peptide into a four-stranded β-sheet structure. *Proteins Struct. Funct. Bioinform.* 65:877–888.
16. Gnanakaran, S., R. Nussinov, and A. E. Garcia. 2006. Atomic-level description of amyloid β-dimer formation. *J. Am. Chem. Soc.* 128:2158–2159.
17. Lei, H., C. Wu, Z. Wang, and Y. Duan. 2006. Molecular dynamics simulations and free energy analyses on the dimer formation of an amyloidogenic heptapeptide from human β2-microglobulin: implication for the protofibril structure. *J. Mol. Biol.* 356:1049–1063.
18. Pellarin, R., and A. Caflisch. 2006. Interpreting the aggregation kinetics of amyloid peptides. *J. Mol. Biol.* 360:882–892.
19. Reference deleted in proof.
20. Rohrig, U. F., A. Laio, N. Tantalo, M. Parrinello, and R. Petronzio. 2006. Stability and structure of oligomers of the Alzheimer peptide a β(16–22): from the dimer to the 32-mer. *Biophys. J.* 91:3217–3229.

21. Melquiond, A., N. Mousseau, and P. Derreumaux. 2006. Structures of soluble amyloid oligomers from computer simulations. *Proteins Struct. Funct. Bioinform.* 65:180–191.
22. Fawzi, N. L., Y. Okabe, E. H. Yap, and T. Head-Gordon. 2007. Determining the critical nucleus and mechanism of fibril elongation of the Alzheimer's Aβ(1–40) peptide. *J. Mol. Biol.* 365:535–550.
23. Fogolari, F., A. Corazza, P. Viglino, P. Zuccato, L. Pieri, P. Faccioli, V. Bellotti, and G. Esposito. 2007. Molecular dynamics simulation suggests possible interaction patterns at early steps of β(2)-microglobulin aggregation. *Biophys. J.* 92:1673–1681.
24. Demarco, M. L., and V. Daggett. 2007. Molecular mechanism for low ph triggered misfolding of the human prion protein. *Biochemistry.* 46:3045–3054.
25. Melquiond, A., J. C. Gelly, N. Mousseau, and P. Derreumaux. 2007. Probing amyloid fibril formation of the NFGAIL peptide by computer simulations. *J. Chem. Phys.* 126:065101.
26. Palyanov, A. Y., S. V. Krivov, M. Karplus, and S. F. Chekmarev. 2007. A lattice protein with an amyloidogenic latent state: stability and folding kinetics. *J. Phys. Chem. B.* 111:2675–2687.
27. Cheon, M., I. Chang, S. Mohanty, L. M. Luheshi, C. M. Dobson, M. Vendruscolo, and G. Favrin. 2007. Structural reorganization and potential toxicity of oligomeric species formed during the assembly of amyloid fibrils. *PLoS Comp. Biol.* 3:1727–1738.
28. Nguyen, P. H., M. S. Li, G. Stock, J. E. Straub, and D. Thirumalai. 2007. Monomer adds to preformed structured oligomers of a β-peptides by a two-stage dock-lock mechanism. *Proc. Natl. Acad. Sci. USA.* 104:111–116.
29. Raman, E. P., T. Takeda, V. Barsegov, and D. K. Klimov. 2007. Mechanical unbinding of a β-peptides from amyloid fibrils. *J. Mol. Biol.* 373:785–800.
30. Soto, P., M. A. Griffin, and J. E. Shea. 2007. New insights into the mechanism of Alzheimer amyloid-β- fibrillogenesis inhibition by *n*-methylated peptides. *Biophys. J.* 93:3015–3025.
31. Takeda, T., and D. K. Klimov. 2007. Dissociation of a β(16–22) amyloid fibrils probed by molecular dynamics. *J. Mol. Biol.* 368:1202–1213.
32. Fawzi, N. L. 2008. Protofibril assemblies of the Arctic, Dutch, and Flemish mutants of the Alzheimer's A β(1–40) peptide. *Biophys. J.* 94:2007–2016.
33. Meli, M., G. Morra, and G. Colombo. 2008. Investigating the mechanism of peptide aggregation: insights from mixed Monte Carlo-molecular dynamics simulations. *Biophys. J.* 94:4414–4426.
34. Song, W., G. H. Wei, N. Mousseau, and P. Derreumaux. 2008. Self-assembly of the β2-microglobulin NHVTLSQ peptide using a coarse-grained protein model reveals β-barrel species. *J. Phys. Chem. B.* 112:4410–4418.
35. Itoh, S. G., and Y. Okamoto. 2008. Amyloid-β(29–42) dimer formations studied by a multicanonical-multioverlap molecular dynamics simulation. *J. Phys. Chem. B.* 112:2767–2770.
36. Jang, S., and S. Shin. 2008. Computational study on the structural diversity of amyloid β-peptide (A β(10–35)) oligomers. *J. Phys. Chem. B.* 112:3479–3484.
37. Esposito, L., C. Pedone, and L. Vitagliano. 2006. Molecular dynamics analyses of cross-β-spine steric zipper models: β-sheet twisting and aggregation. *Proc. Natl. Acad. Sci. USA.* 103:11533–11538.
38. Kayed, R., E. Head, T. M. McIntire, S. C. Milton, C. W. Cotman, and C. G. Glabe. 2003. Common structure of soluble amyloid oligomers implies common mechanism of pathogenesis. *Science.* 300:486–489.
39. Fersht, A. R., and V. Daggett. 2002. Protein folding and unfolding at atomic resolution. *Cell.* 108:573–582.
40. Caflisch, A., and M. Karplus. 1994. Molecular-dynamics simulation of protein denaturation—solvation of the hydrophobic cores and secondary structure of barnase. *Proc. Natl. Acad. Sci. USA.* 91:1746–1750.
41. Ladurner, A. G., L. S. Itzhaki, V. Daggett, and A. R. Fersht. 1998. Synergy between simulation and experiment in describing the energy landscape of protein folding. *Proc. Natl. Acad. Sci. USA.* 95:8473–8478.
42. Klimov, D. K., and D. Thirumalai. 2005. Symmetric connectivity of secondary structure elements enhances the diversity of folding pathways. *J. Mol. Biol.* 353:1171–1186.
43. Case, D. A., T. A. Darden, T. E. Cheatham, III, C. L. Simmerling, J. Wang, R. E. Duke, R. Luo, K. M. Merz, B. Wang, D. A. Pearlman, M. Crowley, S. Brozell, V. Tsui, H. Gohlke, J. Mongan, V. Hornak, G. Cui, P. Beroza, C. Schafmeister, J. W. Caldwell, W. S. Ross, and P. A. Kollman. 2004. AMBER, Ver. 8. University of California at San Francisco, San Francisco, CA.
44. Darden, T., D. York, and L. Pedersen. 1993. Particle mesh Ewald: an *N*-log(*N*) method for Ewald sums in large systems. *J. Chem. Phys.* 98:10089–10092.
45. Lwin, T. Z., Q. Lu, and R. Luo. 2006. Force field influences in protein folding simulations. *Protein Sci.* 15:2642–2655.
46. Wang, J., R. M. Wolf, J. W. Caldwell, P. A. Kollman, and D. A. Case. 2004. Development and testing of a general AMBER force field. *J. Comp. Chem.* 25:1157–1174.
47. Rychaert, J. P., G. Ciccotti, and H. J. C. Berendsen. 1977. Numerical integration of Cartesian equations of motion of a system with constraints: molecular dynamics of *n*-alkanes. *Comp. Phys.* 23:327–341.
48. Sedgewick, R. 1992. Algorithms in C++. Addison-Wesley Publishing Company, Reading, MA.
49. Gsponer, J., U. Haberthur, and A. Caflisch. 2003. The role of side-chain interactions in the early steps of aggregation: molecular dynamics simulations of an amyloid-forming peptide from the yeast prion Sup35. *Proc. Natl. Acad. Sci. USA.* 100:5154–5159.
50. Zheng, J., B. Ma, C. J. Tsai, and R. Nussinov. 2006. Structural stability and dynamics of an amyloid-forming peptide GNNQQNY from the yeast prion Sup-35. *Biophys. J.* 91:824–833.
51. Bernstein, S. L., T. Wyttenbach, A. Baumketner, J.-E. Shea, G. Bitan, D. B. Teplow, and M. T. Bowers. 2005. Amyloid β-protein: monomer structure and early aggregation states of Aβ42 and its Pro-19 alloform. *J. Am. Chem. Soc.* 127:2075–2084.
52. Urbanc, B., L. Cruz, F. Ding, D. Sammond, S. Khare, S. V. Buldyrev, H. E. Stanley, and N. V. Dokholyan. 2004. Molecular dynamics simulation of amyloid β dimer formation. *Biophys. J.* 87:2310–2321.